



Cite this: *Phys. Chem. Chem. Phys.*,
2024, 26, 19960

Valence-to-core X-ray emission spectroscopy of transition metal tetrahalides: mechanisms governing intensities†

Christina Roemelt,^a Sergey Peredkov,^a Frank Neese,^b Michael Roemelt^{*c} and Serena DeBeer^{id} ^{*a}

Valence-to-core (VtC) X-ray emission spectroscopy offers the opportunity to probe the valence electronic structure of a system filtered by selection rules. From this, the nature of its ligands can be inferred. While a preceding 1s ionization creates a core hole, in VtC XES this core hole is filled with electrons from mainly ligand based orbitals. In this work, we investigated the trends in the observed VtC intensities for a series of transition metal halides, which spans the first row transition metals from manganese to copper. Further, with the aid of computational studies, we corroborated these trends and identified the mechanisms and factors that dictate the observed intensity trends. Small amounts of metal p contribution to the ligand orbitals are known to give rise to intensity of a VtC transition. By employing an LCAO (linear combination of atomic orbitals) approach, we were able to assess the amount of metal p contribution to the ligand molecular orbitals, as well as the role of the transition dipole moment and correlate these factors to the experimentally observed intensities. Finally, by employing an ano (atomic natural orbital) basis set within the calculations, the nature of the metal p contribution (3p vs. 4p) was qualitatively assessed and their trends discussed within the same transition metal halide series.

Received 5th March 2024,
Accepted 23rd June 2024

DOI: 10.1039/d4cp00967c

rsc.li/pccp

Introduction

Transition metals play key structural and functional roles in biological processes,^{1–4} catalytic transformations,⁵ as well as in environmental⁶ and material science.⁷ Understanding the geometric and electronic structure changes that occur at transition metals during various processes is thus of broad general interest. To this end, a wide variety of spectroscopic methods (e.g. EPR, vibrational and optical spectroscopy) have been utilized by the broader scientific community and in recent years there has been increasing interest in the element selective manifold of spectroscopy. In this regard, X-ray absorption (XAS) and X-ray emission spectroscopy (XES) provide insight into the geometric and electronic structure of the metal center.^{8–16} XES, in particular, has seen increased applications in recent years

due to the availability of both synchrotron and laboratory setups to perform these measurements.¹⁷ Submitting a sample to high incident energy leads to ionization of a 1s electron of a nucleus (in this context, a transition metal) and an excited state featuring a 1s core hole. This excited state can undergo several decay processes where the 1s core hole is filled with electrons from higher shells, accompanied by the emission of energy in form of X-ray photons or photoelectrons. In the case of a 1s core hole the intensity of the observed emission spectra are dominated by electric dipole allowed np to 1s transitions.¹¹ Fig. 1 shows the K β mainline XES of a Mn complex in which the intense feature results from a 3p \rightarrow 1s transition, which is split by 3p–3d exchange in the final state. As such, K β mainline XES is indicative of the spin state of a system, with the K $\beta_{1,3}$ and K β'' peaks moving closer together with a decreasing number of unpaired spins at the metal center.⁹

To higher energy and with much weaker intensity are the so-called valence-to-core (VtC) XES features (Fig. 1, enhanced inset). VtC XES corresponds to transitions from mainly ligand based ns and np orbitals into the metal 1s orbital, which gain intensity from a small amount of metal np mixing, imparting dipole allowed character to these transitions.^{18,19} The VtC spectra are often comprised of two main features, the low intensity K β'' peak, corresponding to ligand ns \rightarrow metal 1s transitions, and the more intense K $\beta_{2,5}$ peak, corresponding to

^a Max Planck Institute for Chemical Energy Conversion, Stiftstr. 34-36, 45470 Mülheim an der Ruhr, Germany. E-mail: serena.debeer@cec.mpg.de

^b Max-Planck-Institut für Kohlenforschung, Kaiser-Wilhelm-Platz 1, 45470 Mülheim an der Ruhr, Germany

^c Humboldt University Berlin, Brook-Taylor-Str. 2, 12489 Berlin, Germany. E-mail: michael.roemelt@hu-berlin.de

† Electronic supplementary information (ESI) available: Mainline and VtC fits of experimental spectra, comparison between Loewdin and LCAO p contribution, comparison of LCAO 3p and 4p contribution. See DOI: <https://doi.org/10.1039/d4cp00967c>



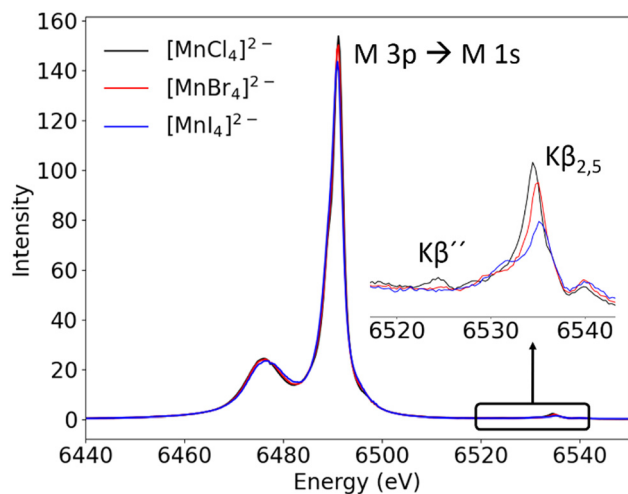


Fig. 1 General shape of X-ray emission spectra (VtC region: enhanced inlet).

ligand $np \rightarrow$ metal $1s$ transitions.^{9,20} The number, intensities and shifts of the VtC features are sensitive to metal ligand bond length (and hence indirectly metal spin state), as well as the identity, ionization state and protonation state of the bound ligands.¹⁹ Previous studies show that these transitions gain intensity by admixture of metal $3p$ and $4p$ orbitals to the filled ligand orbitals.^{9,11,19–27} Several studies have addressed the nature of p contribution (metal $3p$ vs. metal $4p$). However, orbitals are not physical observables but mathematical constructs which were designed to describe the probabilities of where the electrons of a system are located. Therefore, any quantitative assessment is obstructed: the description of orbitals (for example their principal quantum numbers) *via* computational methods always depends on the level of theory that is chosen. Thus, determination of the amount of metal $3p$ vs. metal $4p$ contribution will always be a function of the theory that was applied. In a previous study by our group,¹⁹ a clear dependence between intensity and metal–ligand bond distance was observed when systematically elongating the Fe–Cl bond lengths of an otherwise identical iron complex. Elongation of the Fe–Cl bond leads to a decrease in orbital overlap and thus, to a decrease in p admixture and VtC intensity. The amount of $3p$ and $4p$ contribution was assessed with the aid of calculations employing an *ano* (atomic natural orbital) basis set, where it was found that both $3p$ and $4p$ orbitals contribute to the VtC MO's.

In a previous report from our research group²¹ on a series of Fe complexes, it was corroborated that the intensities associated with the VtC transitions are governed by the overlap between metal and ligand orbitals, as well as the symmetry of this overlap, since only transitions with orbitals of the same symmetry exhibit spectral intensity. The amount of metal p contribution was determined *via* Loewdin population analysis. It was postulated that the total p contribution to all occupied orbitals should sum up to a total of 1200% if only $2p$ and $3p$ orbitals (spin up and spin down) contribute. However, the obtained values for the total p contribution were found to be well above 1200% and metal p admixture to the VtC transition MO's is thus attributed to $4p$ orbitals. In further studies, not

only the amount of p admixture but also the transition dipole moment was taken into consideration when investigating the mechanisms contributing to intensity.²² A detailed analysis of Mn and Fe VtC areas was performed, since it was found that the calculated VtC areas for Mn are always larger than those for Fe at a given bond length. The role of the transition dipole moment was assessed by decomposition into a local (metal np to metal $1s$) and nonlocal (ligand orbitals to metal $1s$) part. The local part of the transition dipole moment was here obtained by atomic calculations for the respective M^{2+} atoms but no clear assignment of $3p$ vs. $4p$ contributions was made. It was found that the reason for higher Mn VtC areas than Fe VtC areas is a subtle interplay of different values for the local transition dipole moments, different amounts of np contribution, as well as a distortion of the metal p orbitals in molecular environment as compared to the atomic calculations.

In a subsequent study²³ the valence molecular orbitals were treated as a linear combination of metal $4p$ and ligand MO's. It was found that no simple linear relationship can be found when correlating metal $4p$ contribution in combination with the respective transition dipole moment ($4p \rightarrow 1s$) to the observed oscillator strengths of the transitions. When taking into consideration metal $3p$ admixture, it was determined that while it is mostly the $4p$ orbitals contributing to the shape of the VtC MO's, it seems to be the $3p$ orbitals in combination with their transition dipole moments ($3p \rightarrow 1s$) which contribute mostly to the observed intensities.

Despite several previous investigations on the intensity contributions to the VtC XES, to our knowledge, these trends have never been investigated across a systematic series that spans the first row transition metals. Within this project, our research focuses on gaining insight in the experimentally observed trends in intensities within the Mn–Cu halide series $[MX_4][NEt_4]_2$, providing experimental data on the two series featuring varying metal/constant halide and constant metal/ varying halide. Further, computational studies were conducted in order to corroborate the observed trends and to investigate in detail the role of metal p contribution, as well as the transition dipole moments contributing to the mechanisms which govern the VtC intensities across these series.

Experimental section

Sample preparation

All investigated compounds ($[MnCl_4][NEt_4]_2$, $[MnBr_4][NEt_4]_2$, $[MnI_4][NEt_4]_2$, $[FeCl_4][NEt_4]_2$, $[FeBr_4][NEt_4]_2$, $[CoCl_4][NEt_4]_2$, $[CoBr_4][NEt_4]_2$, $[NiCl_4][NEt_4]_2$, $[NiBr_4][NEt_4]_2$, $[CuCl_4][NEt_4]_2$ and $[CuBr_4][NEt_4]_2$) were synthesized according to literature procedure.²⁸ XES data were obtained on solid state samples (without any dilution) which were ground to fine powder and sealed into 1 mm aluminum samples holders using 38 μ m Kapton tape.

XES data collection

XES data were collected at the PINK tender X-ray beamline at BESSY II.²⁹ The beam size of all measurements was $30 \times$



500 μm FWHM ($V \times H$). The incoming photon flux was about 10^{13} ph s^{-1} . The FWHM values of the excitation energies decrease from 120 eV to 110 eV to 100 eV for excitation energies of 7.3 keV to 8.0 keV to 9.5 keV, respectively. The spectra were recorded by the use of a dispersive von Hamos spectrometer (bending radius $R = 250$ mm) equipped with an Eiger2 R 500 K ($75 \mu\text{m} \times 75 \mu\text{m}$ pixel size, 512×1030 pixels) detector. The dispersive spectrometer records the entire energy range of an XES spectrum simultaneously. Hence no energy scanning is needed. The beam was scanned over the sample and the signal was averaged. For all samples scan speeds of 50 or $100 \mu\text{m s}^{-1}$ were utilized for which no time dependent changes in the spectra were observed. Calibration of the energy scale was done by measuring suitable reference foils for each transition metal (see Table 1). The PINK beamline in high-flux mode uses a multilayer monochromator with a large passing energy band (≈ 100 eV) without access to monochromatic light.

Therefore, emission lines from reference samples are used for calibration. For the energy calibration procedure two or more emission lines visible by a detector under steady state conditions are needed. The calibration procedure is described in more detail elsewhere.²⁹ Energies were translated into Bragg angles and a fit with tangential function was applied. The samples were continuously scanned within the X-ray beam in order to reduce and evenly distribute the absorbed dose. The samples were scanned at different rates depending on the rate of sample damage. For all samples a scan speed was utilized for which no time dependent changes in the spectra were observed. The estimated total spectral broadening is calculated via $\sqrt{(K_{\text{levelwidth}})^2 + (\text{Spectrometer_resolution})^2}$ where $K_{\text{levelwidth}}$ is the natural broadening of K shell spectral features.³¹

Data processing

The raw data obtained at the PINK beamline were processed using an in-house developed Python script. First, the spectra were preliminarily normalized to the same total to simplify the handling of fitting values during the fit process. Then, a baseline correction is performed where the baseline is fit with one or two broad Pearson functions. In addition, impurities, if present, are also fit with Pearson functions. Fits were performed using the Lmfit package in Python.³² During the fit, the mainline and VtC region are masked (Fig. 2, left, masked region is highlighted in grey) and only the region before the mainline and the last 10 eV of the spectrum are used as fit points. In order to achieve consistency among all investigated species, the masking area is kept constant within a given metal series.

As introduced *vide supra*, the mainline peak corresponds to metal 3p to 1s transitions and is, for our investigated compounds, around two orders of magnitude more intense than the VtC features which gain intensity only by small amounts of metal np admixture. With the total area normalized to 1000 units, the observed VtC areas range from ~ 4 –8 units. Therefore, in order to compare absolute areas, it is crucial to define the peak regions in a consistent fashion, especially when comparing the areas of different metal series to each other. Therefore, the mainline onset (that is, the beginning of the mask region) is defined as that position on the energy axis where the intensity of the mainline feature of a normalized spectrum rises above an intensity of $I > 0.05$. Everything before that position is baselined to a value of zero while everything that is masked maintains intensity. The baseline and, if present, impurities are then subtracted from the spectrum and the spectra were renormalized to a total area of 1000, so that only the mainline and VtC features contribute to the total area

Table 1 VtC XES measurement parameters

Measured element	Excitation energy, keV	FWHM (excitation energy), eV	Analyzer reflection	Estimated spectral broadening, eV	Energy calibration ^a	
					Emission line	Energy, eV/Bragg angle
Mn	7.3	120	Ge(440) 70.5°–78.8°	1.4	Fe K α_1	6404.01/75.45°
					Fe K α_2	6391.03/75.89°
Fe	8	110	Si(440) 62.0°–69.6°	1.4	Co K α_1	6930.38/68.71°
					Co K α_2	6915.54/69.03°
					Fe K β	7058.18/66.19°
Co	9.5	100	Si(620) 68.1°–76.3°	1.7	Ni K α_1	7478.26/74.89°
					Ni K α_2	7461.04/75.38°
					Co K β	7649.45/70.7°
Ni	9.5	100	Si(444) 68.8°–76.8°	1.7	Ta L α_1	8146.1/76.13°
					Ni K β	8264.66/73.12°
					Tb L α_1 Si(333) ^b	6272.8/71.01°
					Tb L α_2 Si(333) ^b	6238.0/71.96°
Cu	9.5	100	Si(444) 60.7°–68°	1.8	Cu K β	8905.42/62.63°
					Zn K α_1	8638.86/66.27°
					Zn K α_2	8615.78/66.62°
					Ho L α_1 Si(333) ^b	6719.8/61.97°

^a Energy calibration for Mn, Fe and Co was performed using energies, asymmetry and FWHM values from Hölzer *et al.*³⁰ Calibration for Ni and Cu was performed using the *X-ray data booklet*. ^b The Tb L α and Ho L α spectra were collected from Si(333) reflection of the same crystal without any rearrangements of the photon beam or the spectrometer.



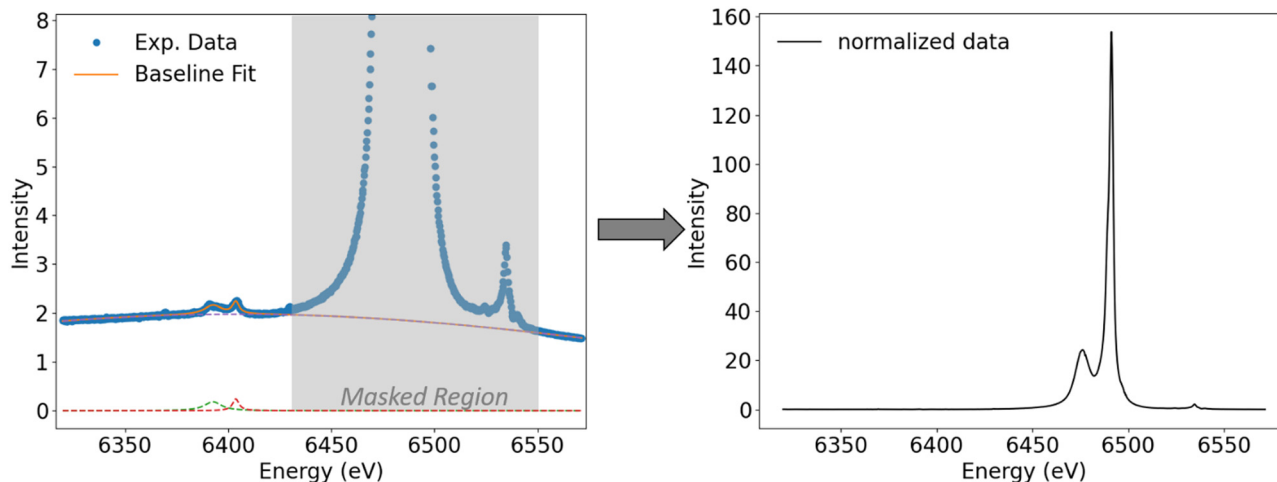


Fig. 2 Fit of the baseline and impurities (background traces from energy calibration with Fe foil, see Table 1) for $[\text{MnCl}_4]^{2-}$ where mainline and VtC features are masked. Right: Spectrum after baseline subtraction and renormalization.

(Fig. 2, right). In order to separate the mainline and VtC areas, the mainline tail is subtracted from the VtC region. To achieve this, now the VtC area is masked during fit (Fig. 3, left, marked in grey). The masking area is kept constant within a given metal series to achieve consistency. The mainline tail is then fit with several Pearson functions. In order to ensure consistency among all investigated species, the fit curve (Fig. 3, left: “Mainline Tail Fit”) must not deviate from the normalized data by a value of more than 2% of the most intense VtC peak intensity. Further, the fit curve must not cross the unmasked data (that is, overestimate the data) to give negative fit values (no zero-crossing). Since only a part of the mainline was used for fitting the tail, the need for additional, physically rather irrelevant fit functions (one broad fit with a maximum between mainline and VtC region) was needed in order to fit the data within the boundaries presented. Then, the mainline tail is subtracted from the VtC region and the resulting VtC area is fit with several Pearson functions (Fig. 3, right). For all obtained spectra, 5–8 Pearson functions are needed to sufficiently describe mainline

and VtC data. The FWHMs of the main $\text{K}\beta_{2,5}$ peaks increase from Mn to Cu (2.2 eV to 4.7 eV), in agreement with increasing core hole lifetime broadenings in the same direction. Fits of all mainline tails and VtC peaks can be found in the ESI.† Within the VtC region, the areas of all required fit functions are summed up to yield the total VtC area. Since the total area of mainline and VtC features is set to 1000, the numbers obtained *via* this procedure give the total VtC area as a fraction out of 1000.

Calculations. Calculations were performed using the ORCA 5.0.3 program package.^{33,34} Crystal structure coordinates (as referenced *vide infra*) were used as starting structures for geometry optimizations. Optimizations were performed using the B3LYP functional^{35,36} together with the ZORA-def2-TZVP basis set,³⁷ where relativistic effects were introduced using the Zeroth Order Regular Approximation (ZORA),³⁸ and the SARC/J auxiliary basis set.³⁹ For calculation of transition metal iodides, the SARC-ZORA-TZVP basis set⁴⁰ was assigned to the halide. To estimate the extent of having employed a different basis set for

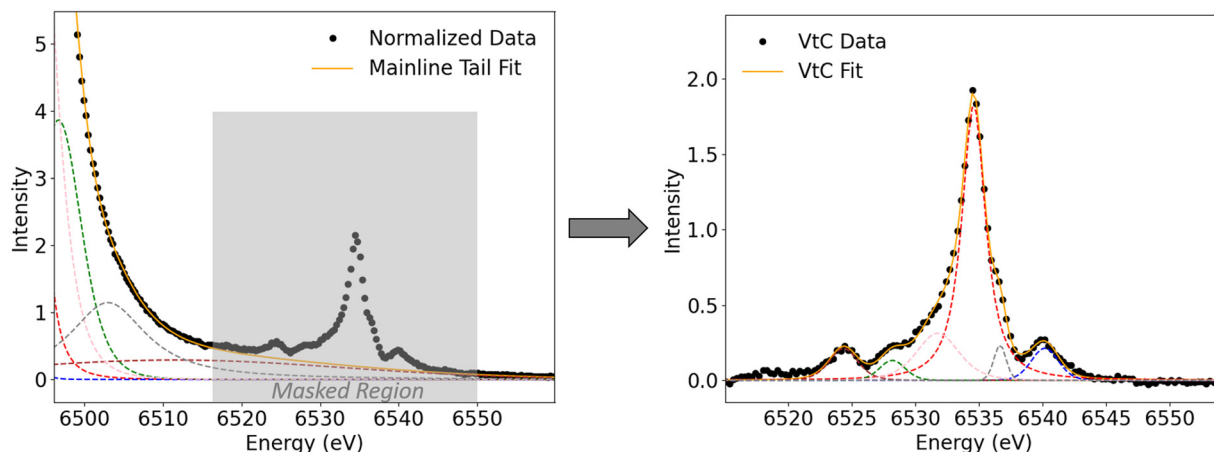


Fig. 3 Left: Mainline tail fit around the VtC region. The masked VtC region is highlighted in grey.



the iodides, all manganese halides were calculated with the exact two-component method X2C for consideration of relativistic effects.⁴¹ It was found that the absolute intensity for the iodide changes slightly, but the general trends in intensities as well as metal p contribution were not affected. Further, dispersion effects were taken into account with Grimme's D3 correction utilizing Becke–Johnson damping (D3BJ).^{42,43} For visualization of molecular orbitals, bond lengths and transition dipole moments, Chimera⁴⁴ and Chemcraft were used. XES calculations were performed employing an established ground state DFT protocol.¹⁹ All input files for optimization and XES calculations can be found attached to this manuscript. The calculated spectra for the transition metal chlorides (Gaussian broadening by 2.5 eV) were shifted such that the most intense VtC features align with the experimental spectra. Then, the corresponding bromides and iodides were shifted by the same value. The effect of quadrupole contributions was determined to be below 2% of the total areas. Since spin orbit coupling (SOC) influences the shape but not the overall intensity of the calculated spectra SOC effects were neglected in order to facilitate the interpretation of orbital compositions. If SOC effects are included, the changes in intensity distribution are found to be negligible and do not affect the correlation between calculated and experimental data.

Results and discussion

Experimental and calculated trends

Experimental and computational data were obtained for a series of transition metal halides $[\text{Net}_4]_2[\text{MX}_4]$ (Table 2) with $M = \text{Mn, Fe, Co, Ni, Cu}$ and $X = \text{Cl, Br and I}$. In the case of the tetraiodides, only the Mn species was experimentally accessible owing to the instability of other iodides or a lack of starting material MI_2 .

All experimentally obtained VtC spectra (Fig. 4 showing the metal chloride series) show the most intense $\text{K}\beta_{2,5}$ peak with shoulders to both sides, originating from transitions from ligand-based np orbitals into the metal 1s orbital. In addition, the $\text{K}\beta''$ features can be found on the lower energy side of the spectrum, originating from transitions from ligand-based ns orbitals into the metal 1s orbital, with the $\text{K}\beta''$ peaks becoming less resolved with increasing nuclear charge of the metal center and decreasing overall intensity of the VtC features. The position of both features on the energy axis depends strongly on the ns/np ionization energies of the respective ligands and move to higher energies for the respective bromides and iodides (see Fig. 1 for the exemplary $[\text{MnCl}_4]^{2-}$). When all experimentally observed peak maxima of the metal chlorides are aligned at 0 eV (Fig. 5), an overall decrease in intensity is observed with increasing Z . Although the $\text{K}\beta''$ peaks become less resolved due to a rather low signal-to-noise ratio and are clearly distinguishable only for manganese and iron, intensity seems to be present for all compounds at roughly the same position relative to their 0 eV $\text{K}\beta_{2,5}$ maximum. Thus, the nature of the transition metal center influences the intensity, but not the relative position of both peak regions. This observation is consistent with the

Table 2 Bond lengths, experimental and calculated VtC areas of the investigated complexes

Compound	exp. VtC area	calcd. VtC area ^a	Av. exp./calcd. bond length [Å]	Ref.
$[\text{MnCl}_4]^{2-}$	8.41	8.41	2.418 / 2.437	45
$[\text{MnBr}_4]^{2-}$	7.79	7.74	2.499 / 2.585	46
$[\text{MnI}_4]^{2-}$	6.65	7.43	2.679 / 2.785	47
$[\text{FeCl}_4]^{2-}$	7.39	7.74	2.324 / 2.386	48
$[\text{FeBr}_4]^{2-}$	6.49	7.06	2.452 / 2.535	49
$[\text{FeI}_4]^{2-}$		6.83	2.640 / 2.731	50
$[\text{CoCl}_4]^{2-}$	6.78	6.83	2.265 / 2.355	45
$[\text{CoBr}_4]^{2-}$	6.26	6.31	2.39 / 2.5	51
$[\text{CoI}_4]^{2-}$		6.16	2.606 / 2.686	52
$[\text{NiCl}_4]^{2-}$	6.00	6.01	2.246 / 2.346	53
$[\text{NiBr}_4]^{2-}$	5.73	5.56	2.368 / 2.484	54
$[\text{NiI}_4]^{2-}$		5.41	2.585 / 2.671	55
$[\text{CuCl}_4]^{2-}$	5.53	5.18	2.236 / 2.338	56
$[\text{CuBr}_4]^{2-}$	4.66	4.65	2.358 / 2.485	57
$[\text{CuI}_4]^{2-}$		4.43	2.644 / 2.674	58

^a Calculated areas are scaled such that experimental and calculated values of the compound with the highest area ($[\text{MnCl}_4]^{2-}$) tally. All calculated values are then scaled by this value ($\text{area}_{\text{calc}} \cdot 0.751$).

energy of the VtC features correlating with the ligand ionization energies.¹⁹

Further, additional peaks on the high energy side of the VtC region are found, which gain in intensity with increasing nuclear charge of the metal and obscure the shape of the $\text{K}\beta_{2,5}$ peaks. As seen in Fig. 4 (the region hatched in grey), these high energy features are located in a region on the energy axis where X-ray absorption pre-edge features for the respective M^{2+} species are typically found. Their observed intensities correlate with the higher incident energies when changing the metal $\text{Mn} \rightarrow \text{Cu}$. Therefore, and in accordance with other studies,^{59–61} these high energy features may be attributed to either vertical or adiabatic double excitation features⁵⁹ (KL or even KM double excitations in case of Cu) and are not considered during the determination of experimental VtC areas. During the fit process, peaks that maximize before they grey area are taken into account when determining the VtC area while peaks which exhibit a maximum within the grey area are neglected.

When changing the halide for a given transition metal, a decrease in the overall intensity (area) accompanied by a shift of the VtC features to higher energies is observed in the chloride \rightarrow bromide \rightarrow iodide direction (see Fig. 1 for the exemplary Mn series). These observations can be rationalized with an elongation of bond lengths (influencing the intensities, *vide infra*) and higher ns/np ionization energies (influencing the energies) in the same direction.

When the experimental and calculated spectra are compared (Fig. 4 representing the chlorides), the relative position of the $\text{K}\beta''$ peaks, where experimentally identifiable, is reasonably well described. The shoulders to the right side of the $\text{K}\beta_{2,5}$ peaks are visibly reproduced by calculations only for the manganese chloride. For all other $[\text{MCl}_4]^{2-}$, the calculated transitions associated with this shoulder merge together with the most intense transitions and cannot be visualized with the applied broadenings. The shoulders on the left side of the $\text{K}\beta_{2,5}$ peaks were not visibly reproduced by the calculations which is consistent with previous studies on Fe chlorides and likely arise from charge transfer



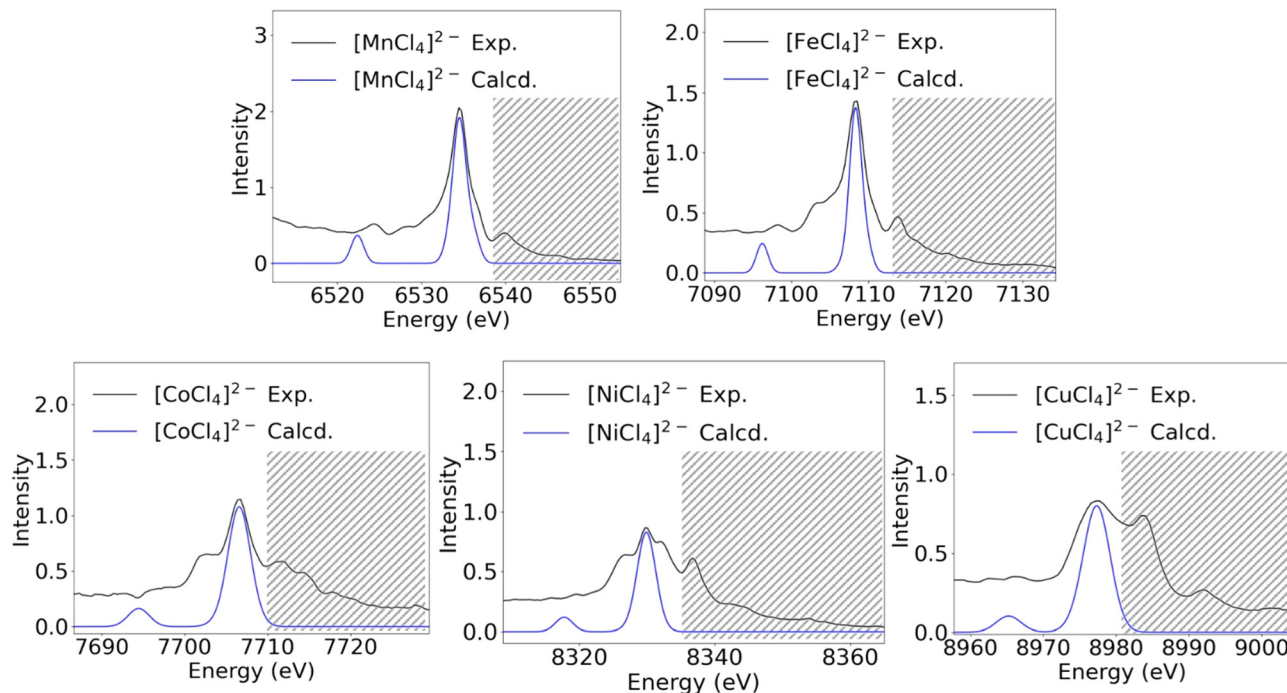


Fig. 4 Experimental (black, smoothed by savgol filter) and calculated (blue, broadening 2.5 eV (Mn, Fe)/3 eV (Co, Ni)/4 eV (Cu)) spectra of the $[MX_4]^{2-}$ series. The areas assigned to double excitation features are hatched in grey and are not considered when determining the VtC area. The calculated spectra were preliminary normalized to a total area of 1000. For optimal visualization the calculated spectra were further scaled by 0.5. We note this is in contrast to the numerical correlations in Table 2, which utilize a scaling factor of 0.751.

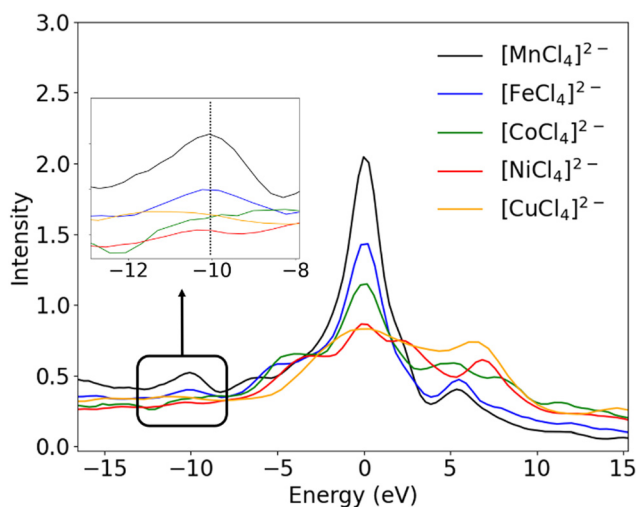


Fig. 5 Normalized experimental spectra with all $K\beta_{2,5}$ maxima aligned at 0 eV.

processes that are not captured in the one-electron DFT approach utilized here.¹⁹ Although this approach does not capture multi excitation or charge transfer processes, it was used here because of its previously established ability to reliably compute VtC features (as referenced in the introduction), its computational feasibility as well as the opportunity to directly assess the relationship between metal p contribution, transition dipole moment and intensity of a transition. When all calculated spectra are aligned at 0 eV (Fig. 6), a

decrease in intensity is observed with increasing Z. Further, the relative position of both peak regions stays constant. Both of these findings agree with the experimentally observed trends (Fig. 5). Lastly, when changing the halide (chloride to bromide to iodide), the calculated decrease in intensity and shift to higher energies also correlates to the experimentally observed findings. Thus, experimentally obtained and calculated values for all VtC areas show excellent correlation (Fig. 7). The observed slight deviations from linearity can mostly be attributed to manual fluctuations in the fit procedure and the rather low signal-to-noise ratio for VtC transitions as compared to other transitions.

For all obtained VtC areas, the previously discussed observations can be summarized as two separate trends: (1) constant metal, varying halide: bond lengths increase and VtC areas decrease (Table 2, marked with dashed arrows); (2) constant halide, varying metal: bond lengths decrease and VtC areas decrease (Table 2, marked with solid arrow). These two trends are discussed in further detail in the following paragraphs. As introduced *vide supra* it has been established that VtC transitions (ligand ns/np to metal 1s) gain intensity by admixture of metal np character into the ligand-based orbitals from which the transitions originate. Therefore, the amount of p contribution to the VtC transitions was quantitatively assessed for all examined complexes by means of computational studies.

Assessment of metal p contribution to the VtC transitions with the aid of DFT

Within this study, we chose an LCAO (linear combination of atomic orbitals) approach to determine the metal p



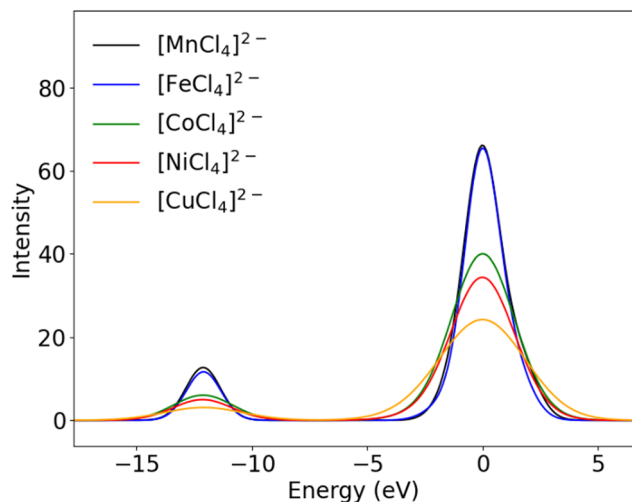


Fig. 6 Calculated spectra (broadening as stated in Fig. 4) with all $K\beta_{2,5}$ peak maxima aligned at 0 eV.

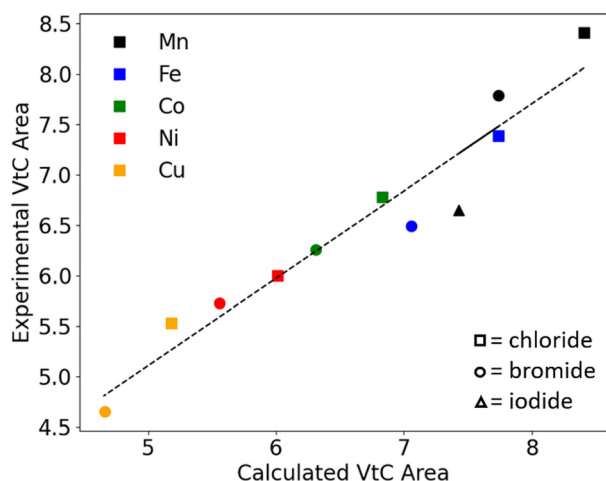


Fig. 7 Correlation between calculated and experimental VtC areas.

contributions to the VtC transitions. Prior to any qualitative and quantitative analysis, it is instructive to reiterate that all observed transitions are modeled as transitions between single-determinantal initial and final states as described originally by Lee *et al.*¹⁹ This means that every transition is associated with a single pair of valence donor and Mn 1s acceptor orbital. Although any state couplings are neglected within this model, it has been successfully applied in many instances.^{22,23,59,62–65}

The amount of p contribution to any molecular orbital can be determined by Loewdin population analysis, as has been done previously as described *vide supra*. However, while Loewdin population analysis provides molecular orbital compositions in terms of atomic orbitals with different angular momenta, *e.g.* s-, p- or d-type orbitals it does not differ between principal quantum numbers, *e.g.* between 3p and 4p contributions. Following an approach presented by Pollock *et al.*²¹ (*vide supra*), the total metal p contribution to all occupied orbitals

can be determined by summing up their metal p contributions as obtained from the Loewdin population. Completely filled metal 2p and 3p orbitals result in a total of 1200% p character (consistent with a total of 12 p-electrons in the 2p and 3p shells). Our values for the total p orbital character of the exemplary $[MnX_4]^{2-}$ series exceed 1200% by almost the exact value which was determined to be the Loewdin p contribution within the VtC transitions (Table 3), thus suggesting that the 4p orbitals contribute to the observed intensity of VtC transitions.

In order to more quantitatively assess the transition metal p contribution to the valence donor orbitals in all VtC transitions, we have applied the LCAO approach, in which it is assumed that any molecular orbital is composed of atomic orbitals, *i.e.*

$$\phi_i(x) = \sum_p c_{ip} \varphi_p(x) \quad (1)$$

Here, the set $\{\phi_i\}$ are molecular orbitals of a given $[MX_4]^{2-}$ species while $\{\varphi_p\}$ are a set of atomic orbitals that originate from an electronic structure calculation of just the central metal M. Importantly, since the “atomic” orbitals $\{\varphi_p\}$ are the result of an electronic structure calculation and not a prefixed set of Gaussian functions, they exhibit the expected angular (s-type vs. p-type *etc.*) and radial (2p vs. 3p *etc.*) features of atomic orbitals. Nevertheless, as is common in molecular electronic structure calculations, both sets of orbitals in eqn (1) are expanded in a set of atom-centered Gaussian-type orbitals (GTOs) $\{\chi_\mu\}$, *i.e.*

$$\phi_i(x) = \sum_\mu c_{\mu i}^{\text{mol}} \chi_\mu(x) \quad (2)$$

$$\varphi_p(x) = \sum_\mu c_{\mu p}^{\text{atom}} \chi_\mu(x) \quad (3)$$

At this point, we would like to note that all molecular and atomic orbitals, as well as their corresponding expansion coefficients in eqn (1)–(3) have been assumed to be real. To ensure that the number of ϕ_i 's and φ_p 's is equal, the electronic structure calculation of just the metal center M has to employ the same GTO basis set as the calculation of the full $[MX_4]^{2-}$ through usage of dummy atoms. Using the expansions in eqn (2) and (3), the coefficients in eqn (1) can be computed through eqn (4):

$$c_{ip} = \sum_{\mu\nu} c_{\mu i}^{\text{mol}} \cdot S_{\mu\nu} \cdot c_{\mu p}^{\text{atom}} \quad (4)$$

or in matrix form in eqn (5):

$$C = C^{\text{mol}, T} S C^{\text{atom}} \quad (5)$$

Table 3 p orbital contribution to VtC transitions and total p orbital contribution to all orbitals for $[MnX_4]^{2-}$ as determined by Loewdin population analysis

Substrate	Mn p contribution to VtC transitions (%)	Total Mn p character (%)
$[MnCl_4]^{2-}$	74.9	1273.2
$[MnBr_4]^{2-}$	72.3	1271.2
$[MnI_4]^{2-}$	69.7	1269.3



where $S_{\mu\nu} = \langle \chi_\mu | \chi_\nu \rangle$ are overlap integrals between the GTO basis functions that are gathered in the overlap matrix \mathbf{S} . The matrices in eqn (5) have been extracted from the ORCA output files with the aid of the `orca_2json` program. With matrix \mathbf{C} at hand, the contribution of a given atomic orbital ϕ_p to molecular orbital ϕ_i is quantified by taking the square of the corresponding matrix element c_{ip} .

Following this LCAO approach, the molecular orbitals of an exemplary $[\text{MnCl}_4]^{2-}$ molecule that are most relevant in terms of VtC intensity comprise only traces of Mn 3p character ($10^{-3}\%$) but considerable contributions from Mn 4p orbitals (3–20%, exact values for all orbitals can be found in the ESI†). By construction, this approach renders 4p contribution as main component because of a clear separation into 3p (occupied) and 4p (unoccupied) orbitals within the atomic calculations. In the following projection of the atomic orbitals onto the molecular orbitals (see eqn (5)), this partitioning is maintained, leaving only 4p contribution to significantly modulate the intensity of the VtC peaks.

Correlation of p contribution and the observed trends

With the amount of metal p contribution determined for all transitions of all compounds, the correlation between p contribution and the intensity of a transition was further investigated.

Constant transition metal center and varying halide. With constant transition metal center and varying halide ($\text{MCl}_4 \rightarrow \text{MBr}_4 \rightarrow \text{MI}_4$), the VtC areas decrease within each metal series (Table 2, marked with dashed arrows). The amount of p admixture is a function of the orbital overlap between the participating metal and ligand orbitals. When changing the halide of a given metal from chloride to bromide to iodide, two factors come to compete: the bond lengths within the complexes elongate while at the same time, the ligand orbitals get more diffuse. The experimentally observed decrease in intensity is associated with a decrease in orbital overlap – thus, less p admixture – between metal and halide. Therefore, the bond elongation seems to outweigh the effect of the more diffuse orbitals. These findings have been corroborated with computational studies on the total Loewdin population analysis of all VtC transitions (Fig. 8). When the experimentally observed bond elongation within the chloride \rightarrow bromide \rightarrow iodide series is considered, the oscillator strength (the combined electric dipole, electric quadrupole and magnetic dipole contributions) decreases and the Loewdin p contribution also decreases in the same direction (solid boxes/arrow). However, when the bond lengths of all halides are fixed to the value of the Mn–Cl bond, an increase in oscillator strength and Loewdin p contribution is observed (hollow boxes/arrow). Thus, with fixed bond lengths, the diffuseness of the corresponding ligand orbitals dictates intensity and p admixture while under realistic conditions, the bond elongation dictates the trend.

However, when plotting the oscillator strength of the single VtC transitions vs. the p contribution determined *via* the LCAO approach, there does not seem to be a clear linear dependence between the intensity of the transition and the amount of metal

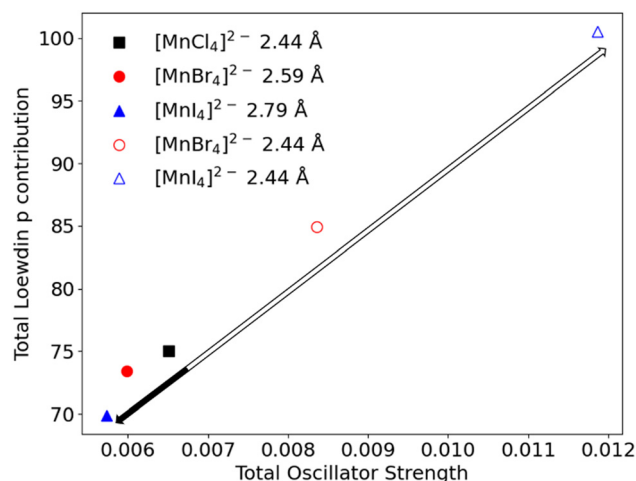


Fig. 8 Total oscillator strength of all VtC transitions vs. total Loewdin p contribution to all VtC transitions for the $[\text{MnX}_4]^{2-}$ series. The solid boxes and arrow show the trend for elongated bond lengths (Cl \rightarrow Br \rightarrow I) while the hollow boxes and arrow show the trend when Mn–Cl, Mn–Br and Mn–I bond lengths are fixed to the value of Mn–Cl.

p contribution. In Fig. 9, we examine the correlation between the oscillator strength and p contributions for both single transitions (left) and for different spectral regions (right). The left panel visualizes the non-linear behavior through a plot of the predicted VtC oscillator strengths of $[\text{MnCl}_4]^{2-}$ vs. the corresponding metal p contributions. Particularly the transitions in the $\text{K}\beta''$ region (six clustered transitions marked with a star) feature a significant amount of Mn p contribution while exhibiting comparably low intensities. A very similar distribution pattern was also observed for the single transitions when the amount of p admixture was determined by Loewdin population analysis (for comparison, see ESI†).

Notwithstanding the lack of linear correlation, a few noteworthy observations can be made when the transitions of the $\text{K}\beta''$ and $\text{K}\beta_{2,5}$ regions of the $[\text{MnX}_4]^{2-}$ series are considered separately and compared to the sum of all transitions (Fig. 9, right panel). In the $\text{K}\beta''$ region (marked in yellow), oscillator strength as well as p contribution decrease in the series chloride \rightarrow bromide \rightarrow iodide. In contrast, the total Mn p contribution to donor orbitals associated with transitions in the $\text{K}\beta_{2,5}$ region (marked in grey) increases with decreasing intensity. These opposing trends can be rationalized by looking at the shape of the participating orbitals. In agreement with experimental evidence,^{45–47} the calculated Mn–X bond length increases from chloride to bromide to iodide by an average of 1.48 Å and 2.0 Å, respectively. However, the character of the donor orbitals corresponding to the transitions in the two aforementioned spectral regions differ (halide ns for the $\text{K}\beta''$ peaks, halide np for the $\text{K}\beta_{2,5}$ peaks). The overlap between ligand ns vs. ligand np orbitals with Mn 3p and 4p orbitals was quantified according to eqn (1)–(5). The overlap of both ligand ns and np orbitals with the manganese 3p orbitals (Table 4, first column) was found to decrease upon bond elongation.

As described above though, the Mn 3p orbitals were found to contribute only marginally to the total Mn p admixture. The



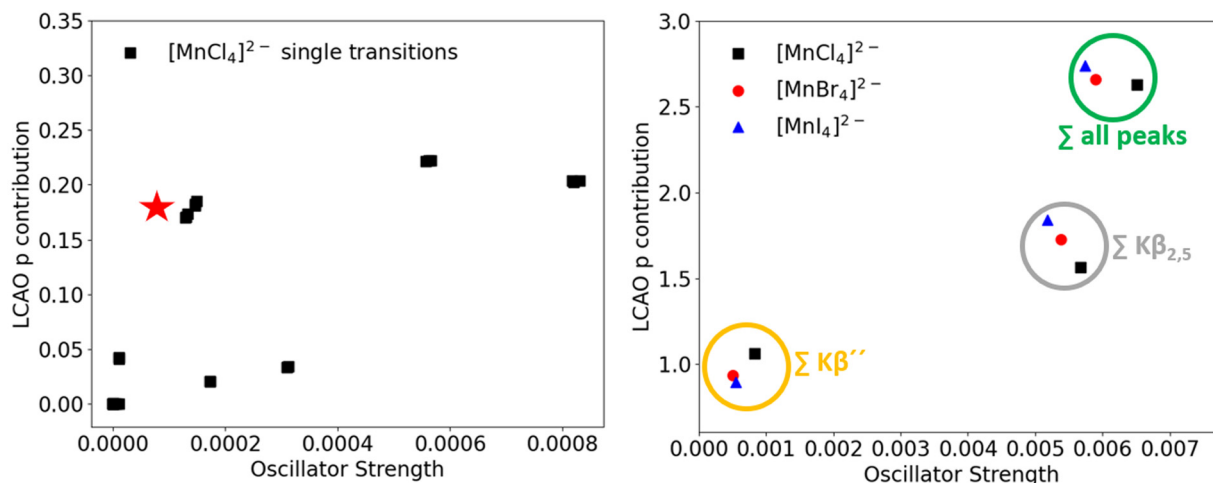


Fig. 9 Mn p contribution in donor orbitals vs. oscillator strength of each VtC transition of $[\text{MnCl}_4]^{2-}$ (left) and summarized p vs. oscillator strength in different peak regions in all investigated manganese species (right).

overlap between the Mn 4p and ligand ns orbitals (Table 4, second column) was also found to decrease, as expected from Fig. 9. Interestingly, the Mn 4p/ligand np overlap was now found to increase with increasing bond length, again as assumed from Fig. 9. Thus, due to the nodal plane inherent to the p orbitals, the overlap of the more diffuse Mn 4p orbitals with the ligand np orbitals seems to maximize at a longer bond length rather than the shortest.

Finally, the total p contribution obtained by our LCAO analysis to all VtC transitions (Fig. 9, right, marked in green) increases from $[\text{MnCl}_4]^{2-}$ to $[\text{MnI}_4]^{2-}$, opposing the expected trend and the trend obtained *via* Loewdin population analysis. Before elaborating on these observations in more detail, the correlation of p contribution and oscillator strength for the series with other metal centers is assessed.

Varying metal center. When varying the metal center ($\text{MnX}_4 \rightarrow \text{FeX}_4 \rightarrow \text{CoX}_4 \rightarrow \text{NiX}_4 \rightarrow \text{CuX}_4$), the experimental and calculated VtC areas were found to decrease while the bond lengths also decrease with constant halide (Table 2, solid arrow). Investigation of the correlation of p contribution as determined *via* the LCAO approach and the oscillator strengths reveals that the same trends as for the $[\text{MnX}_4]^{2-}$ series are found for all other metal series for the different peak regions (Fig. 10, left). Also, a slight but steady increase in total p admixture was found with decreasing total oscillator strength (Fig. 10: sum over all peaks) when altering the metal center. When investigating in more detail the extent of deviation from linearity between metal p contribution and intensity for single transitions of all transition metals, an overall slight increase towards linearity was found with increasing Z . According to Table 5, the majority of metal p contribution stems from 4p orbitals, but for every VtC transition a small amount of metal 3p contribution is also observed. When going from Mn to Ni, the 4p orbitals remain constant in energy whereas the energy of the 3p orbitals decrease significantly, therefore leading to a slightly modified bonding situation between metal p and “other” atomic orbitals. This, again, influences the amount of bonding

Table 4 Ligand ns/np overlap with manganese 3p and 4p orbitals in MnX_4^{2-}

	Mn 3p–L s/p		Mn 4p–L s/p	
MnCl_4	Cl-3s	0.05	Cl-3s	11.5
	Cl-3p	0.36	Cl-3p	17.0
MnBr_4	Br-4s	0.04	Br-4s	10.0
	Br-4p	0.34	Br-4p	18.1
MnI_4	I-5s	0.03	I-5s	9.3
	I-5p	0.28	I-5p	18.8

and antibonding nature of interactions and therefore the amount of positive or negative interference (and therefore deviation from linearity) for the different transition metals (*vide infra*). Copper shows slightly different trends than the other metals. The reason is found in the symmetry of the compounds and was corroborated in a study where bond angles were computationally varied between the tetrahedral and square planar limit. While all other metal halides exhibit T_d symmetry with angles close to 109° , the copper halides are distorted with a symmetry closer to D_{4h} and angles of $100/130^\circ$. Due to partly different symmetries of the interacting metal p orbitals (a_{2u} and e_u in D_{4h}) and ligand SALCs (a_{1g} , b_{1g} and e_u in D_{4h}), some transitions lose intensity, leading to the observed deviations for Cu. Thus, the trends discussed in this study can only be generalized for compounds with T_d symmetry. However, preliminary calculations on systems with other symmetries show that non-linear behavior of p contribution and intensity is, to varying extent, inherent to all of them. Thus, the procedure of analysis presented within this study is also applicable to compounds with symmetries other than T_d . Further, in agreement with previous studies on manganese and iron,²² it was found that at the same M–X bond length, the calculated VtC area of manganese is always higher than that of iron, which is higher than cobalt, and likewise for the other



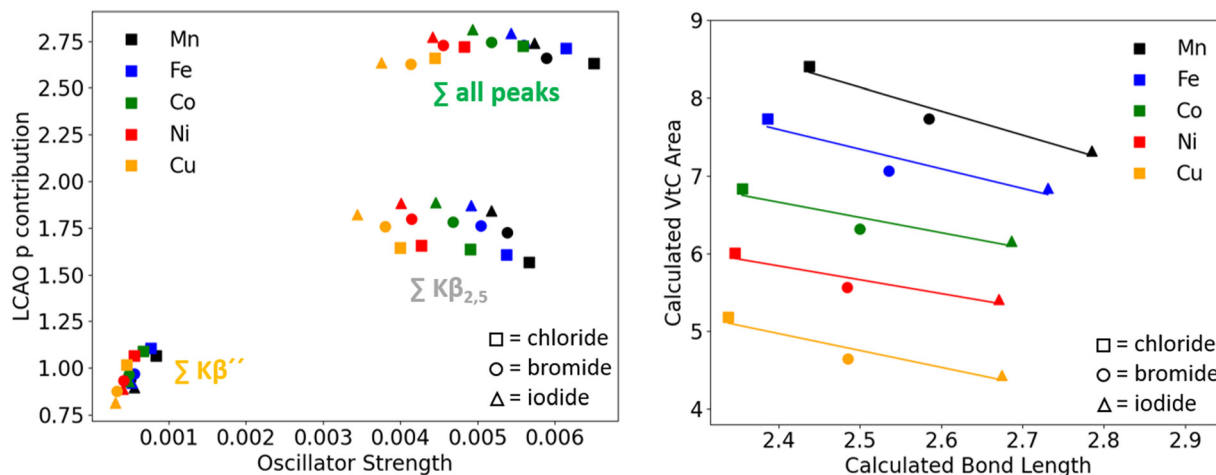


Fig. 10 Left: LCAO p contribution vs. oscillator strength for all investigated compounds. Right: Correlation of calculated bond lengths and calculated VtC areas for all compounds.

Table 5 Total intensities of orbitals ϕ_i to Mn 1s transitions of exemplary $[\text{MnCl}_4]^{2-}$ and their separation into np and "other" contributions as obtained via the LCAO approach of eqn (1)–(5)

Orbital	I_{total}	I_{2p} (%2p)	I_{3p} (%3p)	I_{4p} (%4p)	I_{other} (%other)
$6\alpha^a$	6.94×10^{-4}	6.94×10^{-4} (100.0)	8.13×10^{-9} (0.0)	3.1×10^{-10} (0.0)	-3.1×10^{-9} (−0.0)
7α	6.94×10^{-4}	6.94×10^{-4} (100.0)	8.1×10^{-9} (0.0)	3.0×10^{-10} (0.0)	-3.1×10^{-9} (−0.0)
8α	6.94×10^{-4}	6.94×10^{-4} (100.0)	8.1×10^{-9} (0.0)	2.9×10^{-10} (0.0)	-3.0×10^{-9} (−0.0)
26α	6.06×10^{-5}	-8.1×10^{-9} (−0.0)	6.08×10^{-5} (100.2)	-1.15×10^{-7} (−0.2)	9.68×10^{-9} (0.0)
27α	6.07×10^{-5}	-8.1×10^{-9} (−0.0)	6.08×10^{-5} (100.2)	-1.15×10^{-7} (−0.2)	1.04×10^{-8} (0.0)
28α	6.06×10^{-5}	-8.1×10^{-9} (−0.0)	6.08×10^{-5} (100.2)	-1.15×10^{-7} (−0.2)	1.16×10^{-8} (0.0)
31β	9.46×10^{-8}	1.5×10^{-11} (0.0)	1.45×10^{-8} (15.3)	2.73×10^{-7} (288.0)	-1.92×10^{-7} (−203.3)
34β	5.22×10^{-7}	1.68×10^{-10} (0.0)	3.5×10^{-8} (6.7)	6.77×10^{-7} (129.7)	-1.9×10^{-7} (−36.5)

^a Every orbital carries a spin function, *i.e.* either α or β spin.

metals under consideration (Fig. 10, right panel). These observed trends in calculated correlation between area and bond length, as well as calculated metal p contribution for both the constant metal/constant halide series, which do not seem to readily fit our intuition, together with the obvious lack of a linear correlation between metal p character and predicted oscillator strengths of the single transitions, justify the assumption that there are other factors next to metal p admixture contributing to the observed and calculated intensities. Since the role of the transition dipole moment has been investigated in this regard previously (*vide supra*), we investigated the interplay of p contribution and transition dipole moment in further detail.

Assessment of the role of the transition dipole moment

Due to the observed non-linear behavior of p contribution and intensity and following previously performed studies, the influence of the transition dipole moment was evaluated in more detail (for definition, see ESI†). However, we do not focus solely on the metal p orbitals and their respective transition dipole moments, but take into consideration all atomic orbitals that comprise a molecular orbital. According to Fermi's golden rule the intensity of a given electronic transition from orbital ϕ_i to the Mn 1s orbital is proportional to the square of the

corresponding transition dipole moment, *i.e.*

$$I_i \propto |\langle 1s | \vec{\mu} | \phi_i \rangle|^2 \quad (6)$$

where

$$|\langle 1s | \vec{\mu} | \phi_i \rangle|^2 = |\langle 1s | \mu_x | \phi_i \rangle|^2 + |\langle 1s | \mu_y | \phi_i \rangle|^2 + |\langle 1s | \mu_z | \phi_i \rangle|^2 \quad (7)$$

and

$$|\langle 1s | \mu_x | \phi_i \rangle|^2 = \langle 1s | \mu_x | \phi_i \rangle \langle \phi_i | \mu_x | 1s \rangle \quad (8)$$

Inserting eqn (2) into both terms on the right-hand side of eqn (8) yields

$$\begin{aligned} \langle 1s | \mu_x | \phi_i \rangle \langle \phi_i | \mu_x | 1s \rangle &= \left(\sum_p c_{ip} \langle 1s | \mu_x | \varphi_p \rangle \right) \left(\sum_q c_{iq} \langle \varphi_q | \mu_x | 1s \rangle \right) \\ &= \sum_{pq} c_{ip} c_{iq} T_p^x T_q^x \end{aligned} \quad (9)$$

where T is the transition dipole moment. Considering all x , y and z components of the transition dipole moment, the intensity correlated with each molecular orbital (that is, each transition)



can be calculated *via*

$$I_i = \sum_{pq} c_{ip} c_{iq} \left(T_p^x T_q^x + T_p^y T_q^y + T_p^z T_q^z \right) \quad (10)$$

For our $[\text{MX}_4]^{2-}$ systems, the intensities of every transition were calculated by implementing eqn (10) into a Python script. The values for the orbital coefficients c_{ip} and c_{iq} were obtained according to eqn (3) whereas the values for the transition dipole moments T were obtained from the ORCA output files of our “atomic” XES calculations with extended basis sets (*vide supra*).

The calculated intensities show a perfectly linear correlation within the applied numerical accuracy to the oscillator strengths obtained within the XES output files.

Through eqn (10) the intensity of every transition can be deconvoluted into atomic orbital contributions. We have divided I_i according to

$$I_i = I_{2p}(i) + I_{3p}(i) + I_{4p}(i) + I_{\text{other}}(i) \quad (11)$$

where any term in the double sum of eqn (10) contributes to $I_{2p}(i)$ if index p refers to a Mn 2p orbital. All other contributions are computed analogously. However, it should be noted that the double sum includes many cross terms with different coefficients ($c_{ip} \neq c_{iq}$), a parameter which, to our knowledge, has not been considered within previous studies (*vide supra*). These cross terms can be interpreted as “interference” terms between different atomic orbitals but will all be counted in eqn (11) only according to the index p . Table 5 presents the absolute and relative contributions to a set of transitions which are representative for different spectral regions. Note, the relative contributions can be larger than 100% and even take negative values as will be explained below. Molecular orbitals 6–8 correspond to the manganese $K\alpha$ line, originating exclusively from transitions from the Mn 2p orbitals into the 1s orbital ($I_{2p} = 100\%$). Likewise, orbitals 26–28 correspond to the $K\beta$ mainline, which gains its intensity from Mn 3p to Mn 1s transitions as reflected by I_{3p} values close to 100%. Orbital 31β is a representative donor orbital from the $K\beta''$ region and orbital 34β corresponds to the most intense transition of the $K\beta_{2,5}$ region (Fig. 11). Interestingly, the intensity originating from the admixture of 3p/4p orbitals, combined with their respective transition dipole moments, to these two transitions (I_{3p} and I_{4p}) is calculated to be much higher than the calculated total intensity $I_{31\beta}$ and $I_{34\beta}$ thus accounting for more than 100% relative contribution.

However, these large contributions are partially canceled due to negative interference with “other” orbitals, as indicated by large negative contributions to the intensity from I_{other} . This finding can be interpreted in terms of antiparallel orientation of transition dipole moments for these transitions (*vide infra*). What also becomes apparent is that the intensity originating from Mn 3p/4p orbital contributions for MO 34β is calculated to be about 2.5 times higher than the corresponding intensity for MO 31β , but at the same time the values for negative interference are similar. This observation rationalizes the differences in total intensity as well as the non-linearity previously observed for pure p contribution *vs.* intensity plots. With these

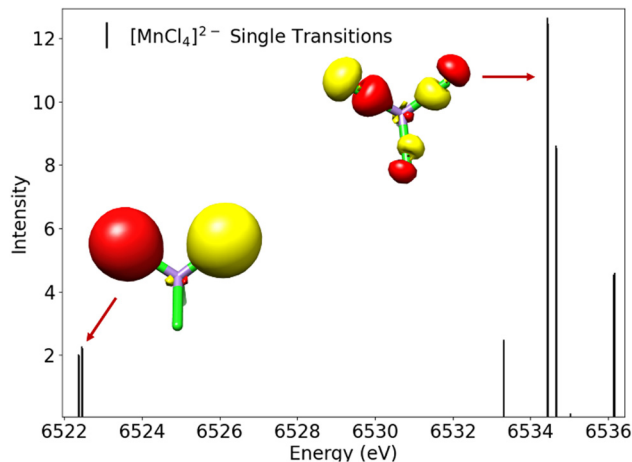


Fig. 11 Selected VtC transitions in the $K\beta''$ (31β) and $K\beta_{2,5}$ region (34β) for detailed analysis.

findings, the correlation between metal np contribution combined with the respective transition dipole moment (p^*T) and the calculated oscillator strength is revisited. Fig. 12 (left panel) shows the correlation of (p^*T) *vs.* oscillator strength for the $[\text{MnCl}_4]^{2-}$ single transitions. Now, a clear linear correlation can be found, where the oscillator strength increases with increasing (p^*T) values. Deviation from total linearity is here accounted for by the negligence of interference with “other” orbitals, as obtained according to Table 5. When the interplay of all orbital contributions (np plus “other”) is plotted, a perfectly linear correlation is obtained.

Further, when assessing the trend within the manganese halide series (Fig. 12, right panel), a decrease in total oscillator strength (sum over all peaks) is accompanied by a decrease in the total (p^*T) values, thus highlighting the importance of taking the transition dipole moment into consideration here.

Finally, when changing the metal center ($\text{Mn} \rightarrow \text{Fe} \rightarrow \text{Co} \rightarrow \text{Ni} \rightarrow \text{Cu}$), the orbitals close to the core of the transition metal center experience an increase in orbital contraction due to an increase in nuclear charge. Thus, it is expected that the respective 1s orbitals (the XES acceptor orbitals) are more contracted and therefore exhibit smaller intrinsic transition dipole moments ($\text{M } np \rightarrow \text{M } 1s$) in the same direction. Fig. 13 shows the correlation between the total (p^*T) and the total oscillator strengths for all transitions for the metal chloride series, where the (p^*T) value decreases in an almost perfectly linear fashion with decreasing oscillator strength.

The origin of negative interference

To assess the nature and origin of the “other” orbitals contributing to the intensity of the VtC transitions in terms of negative (or sometimes even positive) interference, the composition of molecular orbital 31β was analyzed in detail in terms of atomic orbitals according to eqn (1). Moreover, the contribution of every atomic orbital to $I_{31\beta}$ is computed through



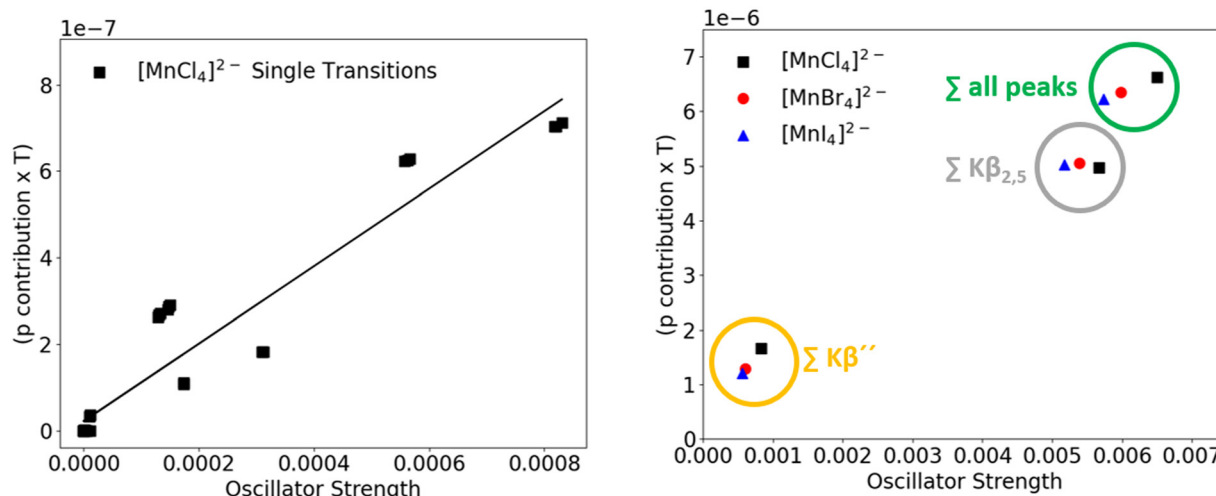


Fig. 12 Correlation of (p^*T) and oscillator strength for the $[\text{MnCl}_4]^{2-}$ single transitions (left) as well as for the total intensities of the manganese halide series (right).

eqn (12):

$$I_p(31\beta) = c_{31\beta,p}^2 \left(T_p^x T_p^x + T_p^y T_p^y + T_p^z T_p^z \right) \quad (12)$$

Table 6 shows the relevant atomic orbitals to MO 31β , as well as their contribution to the total intensity and the direction of their transition dipole moments T^*c where c is the orbital coefficient of the respective atomic orbital. As can be seen in Table 6, MO 31β is comprised of a variety of atomic orbitals, *e.g.* Mn 4p orbitals 15–17, of which only AO 16 contributes significantly (54.7%) to the total intensity. MO 31β , as shown in Fig. 14, is a mostly ligand based molecular orbital with Cl-s character. It was found that several AO's with the respective ligand s character exhibit a high contribution to the shape of the MO but a negligible transition dipole moment, thus not contributing significantly to the total intensity of the transition ($<1\%$). Therefore, these AO's are not considered here. AO 25 as

depicted in Fig. 14 shows a high contribution (18%), as well as a rather high transition dipole moment, thus contributing with 19.9% to the total intensity of the transition. Fig. 14 now demonstrates the interplay of those two orbitals which contribute most to the total intensity, AO 16β (Mn 4p) and AO 25β (ligand s). The black arrows indicate the antiparallel direction of their respective transition dipole moments T , resulting in a smaller value of T in the direction dictated by the Mn 4p orbital when both atomic orbitals are combined in an obviously antibonding fashion (AO 16β + AO 25β , Fig. 14).

The nature of this interaction is captured by the shape of the corresponding molecular orbital 31β , whose shape is also constituted by the antibonding combination of ligand s and metal p orbitals. Thus, negative values for I_{other} as shown in Table 5 can be interpreted in terms of antibonding interactions of the ligand and metal orbitals and might even be used as a means to measure the degree of antibonding character between np and all “other” AO's within any molecular orbital. For a small number of transitions, positive interference between metal np and “other” contributions is observed. This, consequently, is accompanied by bonding interactions between the participating atomic orbitals.

To conclude, bonding interaction between orbitals leads to positive interference between metal p and “other” orbitals and thus positive contribution to the intensity. Accordingly, antibonding interaction leads to negative interference between metal p and “other” orbitals and therefore to a negative contribution to intensity. When metal p contribution and all “other” contributions are quantitatively combined as a sum of their single components, the (T^*c) values for the combined 4p (red) and combined “other” contributions (blue) are shown in Fig. 15, again depicting the antiparallel orientation of both transition dipole moment vectors. Further, combination of the transition dipole moment vectors of both contributions as calculated by this approach adds up to exactly the value of the transition dipole moment of molecular orbital 31β (Fig. 15, magenta) as obtained within the DFT XES calculation output.

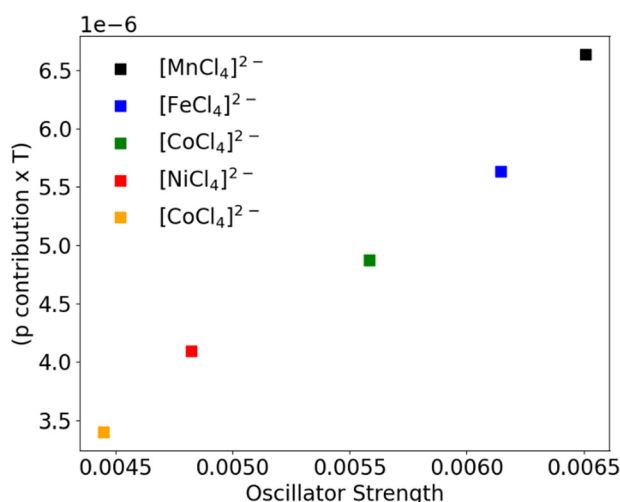
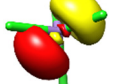
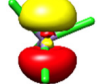

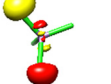
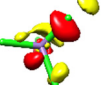
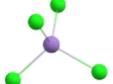


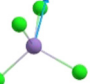
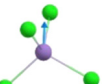
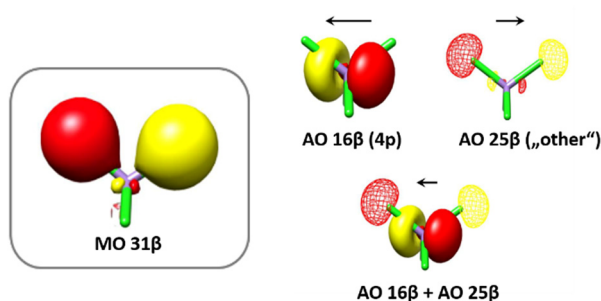


Fig. 13 Correlation of (p^*T) and oscillator strength for the metal chloride series.

Table 6 Atomic orbitals contributing to the intensity of the VtC transition originating from MO 31 β

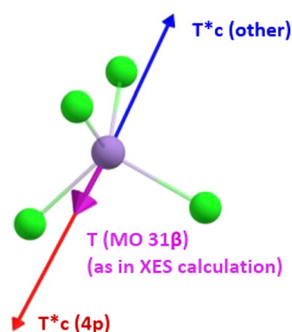
AO	15	16	17	25	35
$c_{31\beta,p}^2$	0.0004	0.1423	0.0396	0.1823	0.052
$c_{31\beta,p}^2 \times T^2$	1.9×10^{-9}	6.1×10^{-7}	1.7×10^{-7}	2.2×10^{-7}	6.6×10^{-8}
Orbital					
Contribution to I_{total}	0.2%	54.7%	15.1%	19.9%	5.9%
T^*c					

**Fig. 14** Interference of the transition dipole moments of a 4p and an "other" orbital in MO 31 β .

It thus becomes apparent that the total intensity of a calculated transition is an interplay of contributions from several atomic orbitals to a molecular orbital and the direction of their respective transition dipole moments.

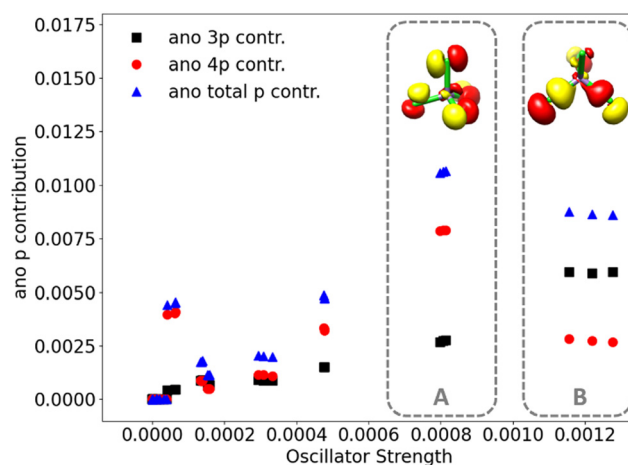
Revisiting the p contribution: 3p or 4p?

Although the LCAO approach for metal p contribution provided us with an explanation on the non-linear behavior between intensity and metal p contribution of a transition, as well as a means to assess the nature and extent of atomic orbital interactions within a molecular orbital, it is not designed for assessing the ratio of metal 3p and metal 4p contribution (*vide*

**Fig. 15** Transition dipole moments (T^*c) of the 4p contributions (red) and "other" contributions (blue) as well as the transition dipole moment of MO 31 β as obtained within the XES calculations (magenta).

supra). Therefore, for the exemplary $[\text{MnCl}_4]^{2-}$ molecule, the metal p contribution was determined by employing an ano (Atomic Natural Orbital) basis set (ANO-RCC-TZP⁶⁶) according to previously published results,¹⁹ where 3p and 4p orbitals can be identified in the basis set and therefore also within the molecular orbitals.

The total manganese p contribution (Fig. 16, blue) was found to be dominated by 3p contribution (Fig. 16, black) when, within a molecular orbital, ligand and metal orbitals interact *via* sigma bonding interactions (peak region B). The more diffuse 4p orbitals (Fig. 16, red) were found to dominate the amount of p contribution in molecular orbitals where metal and ligands interact *via* pi bonding (peak region A). Further, when changing the halide (chloride \rightarrow bromide \rightarrow iodide), metal 4p contributions gain in importance even for those MO's which exhibit sigma interaction between metal and ligand orbitals, which can be rationalized by the more diffuse p orbital character of the heavier halides and thus better interactions with metal 4p orbitals. When the nature of the transition metal center is varied, 4p contributions again increase with increasing effective nuclear charge of the metal center, irrespective of the type of interaction. This is due to the fact that the energetics of the interacting orbitals changes drastically. For the metal

**Fig. 16** Total p contribution (blue) separated into 3p (black) and 4p (red) parts.

chloride series, the energies of ligand s and p orbitals, as well as metal 4 p orbitals was found to maintain rather constant, while the energies of the 3p orbitals decrease linearly with increasing Z, thus promoting 4p contribution.

It has to be noted however that, due to the fact that orbitals are not physical observables, a quantitative analysis of the nature of p contribution is always a function of the employed level of theory and can vary with different sets of unitary transformed molecular orbitals. However, employment of the ano basis set renders a good qualitative picture to assess the nature and trends of the dominating interactions within our transition metal halide series.

Conclusions

Herein a systematic VtC XES study of the first-row transition metal tetrahalides has been performed. The VtC features were investigated with respect to the experimentally observed intensities and changes thereof. The experimentally observed trends with (a) varying halide and (b) varying metal center were corroborated with the aid of computations. Further, employing an LCAO (linear combination of atomic orbitals) approach, the mechanisms which govern these intensities were identified. It was found that there are two main factors whose interplay determines the intensity of each transition within a VtC region. Metal p admixture to the ligand ns and np orbitals, from which these transitions originate, gives intensity to these transitions, and the amount of metal p contribution gives a rough estimate of the intensity of a transition. However, the total intensity of a transition was found to be an interplay of the metal p admixture and the directions of the transition dipole moment vectors of all atomic orbitals that comprise a molecular orbital from which a given transition originates. While for constant metal and varying halide, the amount of metal p contribution roughly dictates the trend of calculated intensities, the effect of the transition dipole moment gains in importance and dictates the general trends in intensities when investigating transition metal complexes with varying metal center. Due to the increasing effective nuclear charge when going from manganese to copper, the metal 1s orbital experiences a greater increase in orbital contraction than the valence orbitals, thus leading to a decrease in the intrinsic transition dipole moment and therefore to reduced intensities. In contrast to previous studies on this topic, we have not considered metal np orbital contributions and ligand orbital contributions with their transition dipole moments separately, but instead investigated the interplay of all atomic orbitals within a molecular orbital by also considering the cross terms. With the introduction of negative interference (or, in other words, a means to determine the extent of antibonding interaction) between np and other orbitals, we were able to assess and explain the non-linearity previously observed for the correlation of p contribution and intensity of a given transition. Lastly, by employing an atomic natural orbital basis set, we were able to qualitatively address the question of metal 3p *versus* metal 4p contribution and their trends within

our transition metal tetrahalide series. It was found that the amount 3p and 4p contributions in $[\text{MnCl}_4]^{2-}$ depends on the type of bonding interactions between ligand and metal center. In case of sigma bonding interactions, 3p contributions dominate, while 4p contributions are the dominating factor for pi interactions. When changing the halide, 4p contributions gain in importance due to more diffuse halide np orbitals. With varying metal center, 4p contributions again gain in importance due to a linear decrease of the energies of the metal 3p orbitals with increasing nuclear charge.

Data availability

All XES raw data, input and xyz files for reproduction of calculations as well as the data necessary for reproduction of the figures within this manuscript can be found online: <https://doi.org/10.17617/3.JECRGR>.

Conflicts of interest

There are no conflicts to declare.

Acknowledgements

CR, SP, FN and SD thank the Max Planck Society for funding. CR thanks the HZBP PINK beamline for the opportunity to measure the samples.

Open Access funding provided by the Max Planck Society.

Notes and references

- 1 C. Van Stappen, L. Decamps, G. E. Cutsail, III, R. Bjornsson, J. T. Henthorn, J. A. Birrell and S. DeBeer, *Chem. Rev.*, 2020, **120**, 5005–5081.
- 2 C.-H. Wang and S. DeBeer, *Chem. Soc. Rev.*, 2021, **50**, 8743–8761.
- 3 P. Gandeepan, T. Müller, D. Zell, G. Cera, S. Warratz and L. Ackermann, *Chem. Rev.*, 2019, **119**, 2192–2452.
- 4 B. M. Hoffman, D. R. Dean and L. C. Seefeldt, *Acc. Chem. Res.*, 2009, **42**, 609–619.
- 5 M. Inoue, H. Tsurugi and K. Mashima, *Coord. Chem. Rev.*, 2022, **473**, 214810.
- 6 J. J. Soldevila-Barreda and N. Metzler-Nolte, *Chem. Rev.*, 2019, **119**, 829–869.
- 7 M. M. Montemore, M. A. van Spronsen, R. J. Madix and C. M. Friend, *Chem. Rev.*, 2018, **118**, 2816–2862.
- 8 M. Bauer, *Phys. Chem. Chem. Phys.*, 2014, **16**, 13827–13837.
- 9 C. J. Pollock and S. DeBeer, *Acc. Chem. Res.*, 2015, **48**, 2967–2975.
- 10 G. E. Cutsail III and S. DeBeer, *ACS Catal.*, 2022, **12**, 5864–5886.
- 11 P. Glatzel and U. Bergmann, *Coord. Chem. Rev.*, 2005, **249**, 65–95.
- 12 L. Cao, X. Liu, X. Shen, D. Wu and T. Yao, *Acc. Chem. Res.*, 2022, **55**, 2594–2603.



- 13 E. Lundgren, C. Zhang, L. R. Merte, M. Shipilin, S. Blomberg, U. Hejral, J. Zhou, J. Zetterberg and J. Gustafson, *Acc. Chem. Res.*, 2017, **50**, 2326–2333.
- 14 M. L. Baker, M. W. Mara, J. J. Yan, K. O. Hodgson, B. Hedman and E. I. Solomon, *Coord. Chem. Rev.*, 2017, **345**, 182–208.
- 15 C. J. Milne, T. J. Penfold and M. Chergui, *Coord. Chem. Rev.*, 2014, **277–278**, 44–68.
- 16 C. Garino, E. Borfecchia, R. Gobetto, J. A. van Bokhoven and C. Lamberti, *Coord. Chem. Rev.*, 2014, **277–278**, 130–186.
- 17 P. Zimmermann, S. Peredkov, P. M. Abdala, S. DeBeer, M. Tromp, C. Müller and J. A. van Bokhoven, *Coord. Chem. Rev.*, 2020, **423**, 213466.
- 18 G. Smolentsev, A. V. Soldatov, J. Messinger, K. Merz, T. Weyhermüller, U. Bergmann, Y. Pushkar, J. Yano, V. K. Yachandra and P. Glatzel, *J. Am. Chem. Soc.*, 2009, **131**, 13161–13167.
- 19 N. Lee, T. Petrenko, U. Bergmann, F. Neese and S. DeBeer, *J. Am. Chem. Soc.*, 2010, **132**, 9715–9727.
- 20 E. Gallo and P. Glatzel, *Adv. Mater.*, 2014, **26**, 7730–7746.
- 21 C. J. Pollock and S. DeBeer, *J. Am. Chem. Soc.*, 2011, **133**, 5594–5601.
- 22 M. A. Beckwith, M. Roemelt, M. N. Collomb, C. DuBoc, T. C. Weng, U. Bergmann, P. Glatzel, F. Neese and S. DeBeer, *Inorg. Chem.*, 2011, **50**, 8397–8409.
- 23 M. U. Delgado-Jaime, S. DeBeer and M. Bauer, *Chemistry*, 2013, **19**, 15888–15897.
- 24 P. Chandrasekaran, K. P. Chiang, D. Nordlund, U. Bergmann, P. L. Holland and S. DeBeer, *Inorg. Chem.*, 2013, **52**, 6286–6298.
- 25 S. N. MacMillan, R. C. Walroth, D. M. Perry, T. J. Morsing and K. M. Lancaster, *Inorg. Chem.*, 2015, **54**, 205–214.
- 26 M. Torres Deluigi, F. M. F. de Groot, G. López-Díaz, G. Tirao, G. Stutz and J. Riveros de la Vega, *J. Phys. Chem. C*, 2014, **118**, 22202–22210.
- 27 K. P. Schwalenstocker, J. Paudel, A. Kohn, C. Dong, K. van Heuvelen, E. Farquhar and F. Li, *Dalton Trans.*, 2016, **45**, 14191–14202.
- 28 N. Gill and F. B. Taylor, *Inorg. Synth.*, 1967, **IX**, 136–142.
- 29 S. Peredkov, N. Pereira, D. Grötzsch, S. Hendel, D. Wallacher and S. DeBeer, *J. Synchrotron Radiat.*, 2024, **31**, 622–634.
- 30 G. Hölzer, M. Fritsch, M. Deutsch, J. Härtwig and E. Förster, *Phys. Rev. A: At., Mol., Opt. Phys.*, 1997, **56**, 4554–4568.
- 31 M. O. Krause and J. H. Oliver, *J. Phys. Chem. Ref. Data*, 1979, **8**, 329–338.
- 32 M. Newville, T. Stensitzki, D. B. Allen, M. Rawlik, A. Ingargiola and A. Nelson, *Lmfit: Non-Linear Least-Square Minimization and Curve-Fitting for Python*, 2016.
- 33 F. Neese, *Wiley Interdiscip. Rev.: Comput. Mol. Sci.*, 2012, **2**, 73–78.
- 34 F. Neese, *Wiley Interdiscip. Rev.: Comput. Mol. Sci.*, 2022, **12**, e1606.
- 35 A. D. Becke, *Phys. Rev. A: At., Mol., Opt. Phys.*, 1988, **38**, 3098–3100.
- 36 C. Lee, W. Yang and R. G. Parr, *Phys. Rev. B: Condens. Matter Mater. Phys.*, 1988, **37**, 785–789.
- 37 F. Weigend and R. Ahlrichs, *Phys. Chem. Chem. Phys.*, 2005, **7**, 3297–3305.
- 38 D. A. Pantazis, X.-Y. Chen, C. R. Landis and F. Neese, *J. Chem. Theory Comput.*, 2008, **4**, 908–919.
- 39 F. Weigend, *Phys. Chem. Chem. Phys.*, 2006, **8**, 1057–1065.
- 40 J. D. Rolfes, F. Neese and D. A. Pantazis, *J. Comput. Chem.*, 2020, **41**, 1842–1849.
- 41 Y. J. Franzke, R. Trefß, T. M. Pazdera and F. Weigend, *Phys. Chem. Chem. Phys.*, 2019, **21**, 16658–16664.
- 42 S. Grimme, J. Antony, S. Ehrlich and H. Krieg, *J. Chem. Phys.*, 2010, **132**, 154104.
- 43 S. Grimme, S. Ehrlich and L. Goerigk, *J. Comput. Chem.*, 2011, **32**, 1456–1465.
- 44 E. F. Pettersen, T. D. Goddard, C. C. Huang, G. S. Couch, D. M. Greenblatt, E. C. Meng and T. E. Ferrin, *J. Comput. Chem.*, 2004, **25**, 1605–1612.
- 45 I. Dhouib, A. Ouasri and Z. Elaoud, *J. Saudi Chem. Soc.*, 2020, **24**, 567–583.
- 46 F. A. Cotton, L. M. Daniels and P. Huang, *Inorg. Chem.*, 2001, **40**, 3576–3578.
- 47 M. Daub, I. Ketterer and H. Hillebrecht, *Zeitschrift für anorganische und allgemeine Chemie*, 2018, **644**, 280–287.
- 48 S. I. P. I. G. Gusakovskaya, N. S. Ovanesyan, N. I. Golovina, R. F. Trofimova, G. V. Shilov and E. A. Lavrent'eva, *Zhurnal Obshchei Khimii*, 1998.
- 49 U. Flörke, E. Akin and G. Henkel, *CCDC 1033638: Experimental Crystal Structure Determination*, 2014, DOI: [10.5517/cc13pl5k](https://doi.org/10.5517/cc13pl5k).
- 50 U. Flörke and A. Ahmida, *CCDC 1571757: Experimental Crystal Structure Determination*, 2017, DOI: [10.5517/ccdc.csd.cc1prjvt](https://doi.org/10.5517/ccdc.csd.cc1prjvt).
- 51 E. Styczeń, Z. Warnke, D. Wyrzykowski, J. Kłak, J. Mroziński and A. Sikorski, *Struct. Chem.*, 2010, **21**, 269–276.
- 52 A. L. Rheingold, L. Doerrer and S. Neville, *CCDC 1503773: Experimental Crystal Structure Determination*, 2016, DOI: [10.5517/ccdc.csd.cc1mgstp](https://doi.org/10.5517/ccdc.csd.cc1mgstp).
- 53 G. D. Stucky, J. B. Folkers and T. J. Kistenmacher, *Acta Crystallogr.*, 1967, **23**, 1064–1070.
- 54 P. G. Jones and H. Thonnessen, *CCDC 611801: Experimental Crystal Structure Determination*, 2006, DOI: [10.5517/ccnjm9](https://doi.org/10.5517/ccnjm9).
- 55 J. A. Golen, A. L. Rheingold, G. Wang and L. Doerrer, *CCDC 781132: Experimental Crystal Structure Determination*, 2014, DOI: [10.5517/ccv6ttn](https://doi.org/10.5517/ccv6ttn).
- 56 T. Kawata, T. Aoyama and S. Ohba, *Acta Crystallogr., Sect. C: Struct. Chem.*, 1993, **49**, 137–139.
- 57 G. L. Starova, M. Y. Skripkin and I. M. Gusev, *Russ. J. Gen. Chem.*, 2010, **80**, 1236–1241.
- 58 R.-Y. Wang, X. Zhang, J.-H. Yu and J.-Q. Xu, *J. Solid State Chem.*, 2019, **269**, 239–245.
- 59 O. McCubbin Stepanic, J. Ward, J. E. Penner-Hahn, A. Deb, U. Bergmann and S. DeBeer, *Inorg. Chem.*, 2020, **59**, 13551–13560.
- 60 H. Lim, M. L. Baker, R. E. Cowley, S. Kim, M. Bhadra, M. A. Siegler, T. Kroll, D. Sokaras, T.-C. Weng, D. R. Biswas, D. M. Dooley, K. D. Karlin, B. Hedman, K. O. Hodgson and E. I. Solomon, *Inorg. Chem.*, 2020, **59**, 16567–16581.



- 61 R. A. Valenza, E. P. Jahrman, J. J. Kas and G. T. Seidler, *Phys. Rev. A*, 2017, **96**, 032504.
- 62 M. U. Delgado-Jaime, B. R. Dible, K. P. Chiang, W. W. Brennessel, U. Bergmann, P. L. Holland and S. DeBeer, *Inorg. Chem.*, 2011, **50**, 10709–10717.
- 63 J. K. Kowalska, A. W. Hahn, A. Albers, C. E. Schiewer, R. Bjornsson, F. A. Lima, F. Meyer and S. DeBeer, *Inorg. Chem.*, 2016, **55**, 4485–4497.
- 64 K. M. Lancaster, K. D. Finkelstein and S. DeBeer, *Inorg. Chem.*, 2011, **50**, 6767–6774.
- 65 K. M. Lancaster, M. Roemelt, P. Ettenhuber, Y. Hu, M. W. Ribbe, F. Neese, U. Bergmann and S. DeBeer, *Science*, 2011, **334**, 974–977.
- 66 B. O. Roos, R. Lindh, P.-Å. Malmqvist, V. Veryazov and P.-O. Widmark, *J. Phys. Chem. A*, 2005, **109**, 6575–6579.

